Supplementary Information

Laser-Architected Vertical Micro-Channel Arrays in Thick Graphene Electrodes for High-Rate Zinc-Ion Hybrid Capacitors

Yudong Wang,[abd]‡ Jun Kang,[bcd]‡ Jixiang Zhang,[a] Yanping Song,[bd] Zhao Li,[bcd] Na Hong,[bcd] Shudong Zhang,[bd] Cui Liu,[bd] Min Xi,*[bd] Zhenyang Wang,[bd] and Nian Li*[bd]*

[a] School of Mechatronics and Vehicle Engineering, Chongqing Jiaotong University, Chongqing 400074, China

[b] Institute of Solid-State Physics, Hefei Institutes of Physical Science, Chinese Academy of Sciences, Hefei, Anhui, 230031, China

[c] Department of Chemistry, University of Science and Technology of China, Hefei, Anhui, 230026, China

[d] Key Laboratory of Photovoltaic and Energy Conservation Materials, Hefei Institutes of Physical Science, Chinese Academy of Sciences, Hefei, Anhui, 230031, China

***Corresponding Authors**

E-mail: zhangjx@cqjtu.edu.cn; minxi@issp.ac.cn; linian@issp.ac.cn;

1. Calculations

1.1 Composite electrode[1]

The areal specific capacitance of the prepared electrode materials was calculated from cyclic voltammetry (CV) curves as the follow equation (S1) and galvanostatic charge-discharge (GCD) curves as the follow equation (S2):

$$C_A = \frac{\int I(v)dv}{A \cdot v \cdot (\Delta V)} \tag{S1}$$

$$C_A = \frac{I \cdot \Delta t}{A \cdot (\Delta V)} \tag{S2}$$

C_A represent the areal specific capacitance (mF/cm^2), $\int I(v)dv$ is the area of the CV curve contained, v is the voltage scan rate (mV/s), ΔV is the applied working potential window (V), A is the active region area of electrode (cm^2), I represent the discharge current (mA), Δt is the discharge time (s).

1.2 Zinc-ion hybrid capacitor

The areal specific capacitance of the assembled Zinc-ion hybrid capacitor (ZHC) was calculated from galvanostatic charge/discharge (GCD) curves as follow equation (S3):

$$C_A = \frac{I \cdot \Delta t}{A \cdot (\Delta V)} \tag{S3}$$

C_A represent the areal specific capacitance (mF/cm^2), ΔV is the applied working potential window (V), A is the geometric area of electrode (cm^2), I represent the discharge current (A), Δt is the discharge time (s).

Additionally, the energy density and power density of the ZHC device was calculated by equation (S4) and equation (S5), respectively.

$$E_A = \frac{\frac{1}{2} \cdot C_A \cdot (\Delta V)^2}{3.6} \tag{S4}$$

$$P_A = \frac{3.6 \cdot E_A}{\Delta t} \tag{S5}$$

Where E_A represent the energy density (μWh/cm^2), P_A represent the power density (mW/cm^2), C_A represent the areal specific capacitance (mF/cm^2), ΔV is the applied working potential window (V), Δt is the discharge time (s).

2. Figures

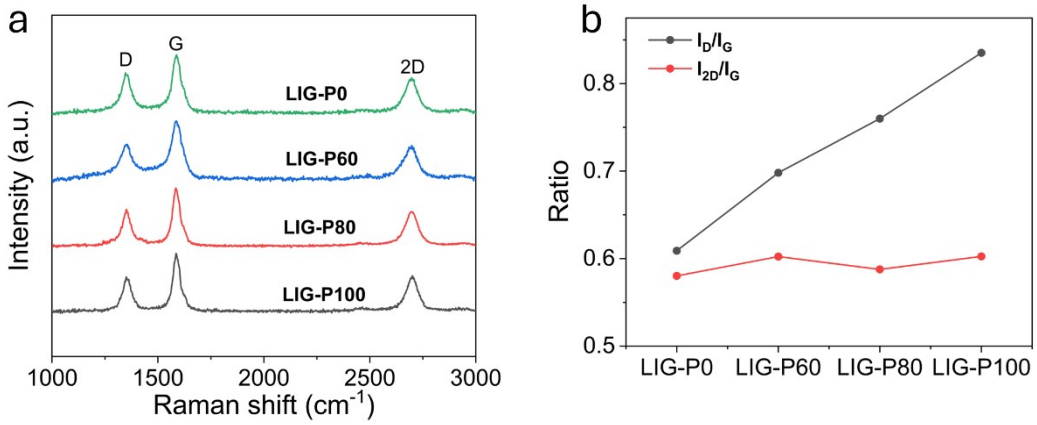

Figure. S1 (a) Raman spectra acquired specifically from the edge regions of the laser-drilled micro-channels for LIG-P0, LIG-P60, LIG-P80, and LIG-P100 electrodes. **(b)** Statistical comparison of the I_D/I_G and I_{2D}/I_G peak intensity ratios.

To investigate the local structural changes induced by the subtractive manufacturing process, Raman characterization was spatially focused on the boundaries of the laser-drilled channels. Unlike the pristine bulk region, the channel edges exhibit a distinct progressive increase in the I_D/I_G ratio from 0.61 (LIG-P0) to 0.84 (LIG-P100). This trend effectively maps the "fingerprint" of the 1064 nm laser ablation, which physically severs the graphene lattice to create vertical voids, thereby generating abundant edge defects and dangling bonds along the channel walls. Notably, the I_{2D}/I_G ratio remains relatively stable, confirming that the laser processing is precise enough to preserve the graphitic stacking order of the surrounding framework. These laser-induced edge defects are functionally pivotal; they serve as extrinsic active sites that can facilitate ion adsorption and enhance surface wettability, effectively activating the interface of the vertical channels for superior electrochemical kinetics.

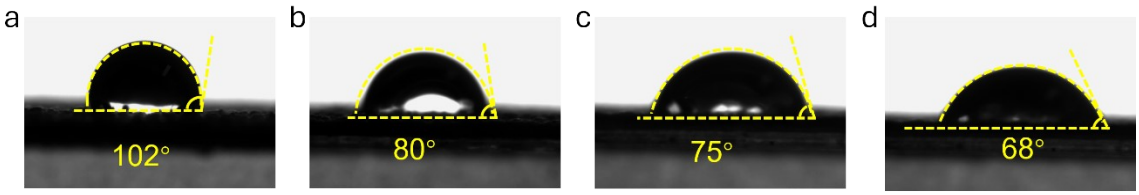

Figure. S2 Static water contact angle measurements of the **(a)** LIG-P0, **(b)** LIG-P60, **(c)** LIG-P80, and **(d)** LIG-P100 electrodes.

The electrolyte infiltration capability was further evaluated via contact angle measurements (***Figure S2***). The pristine LIG-P0 electrode (Panel a) exhibits a relatively hydrophobic nature with a large contact angle, which typically hinders ion transport into deep electrode layers. In sharp contrast, the laser-drilled electrodes (Panels b-d) display a progressive decrease in contact angles as the channel diameter increases. This improved wettability is attributed to a synergistic effect: mechanically, the vertical channels break the surface tension and provide capillary pathways for liquid entry; chemically, the abundant edge defects by laser ablation (as evidenced by Raman spectra in Figure S1) act as hydrophilic sites. This enhanced surface affinity ensures that the aqueous electrolyte can rapidly permeate the thick electrode, reactivating the deep-seated active materials.

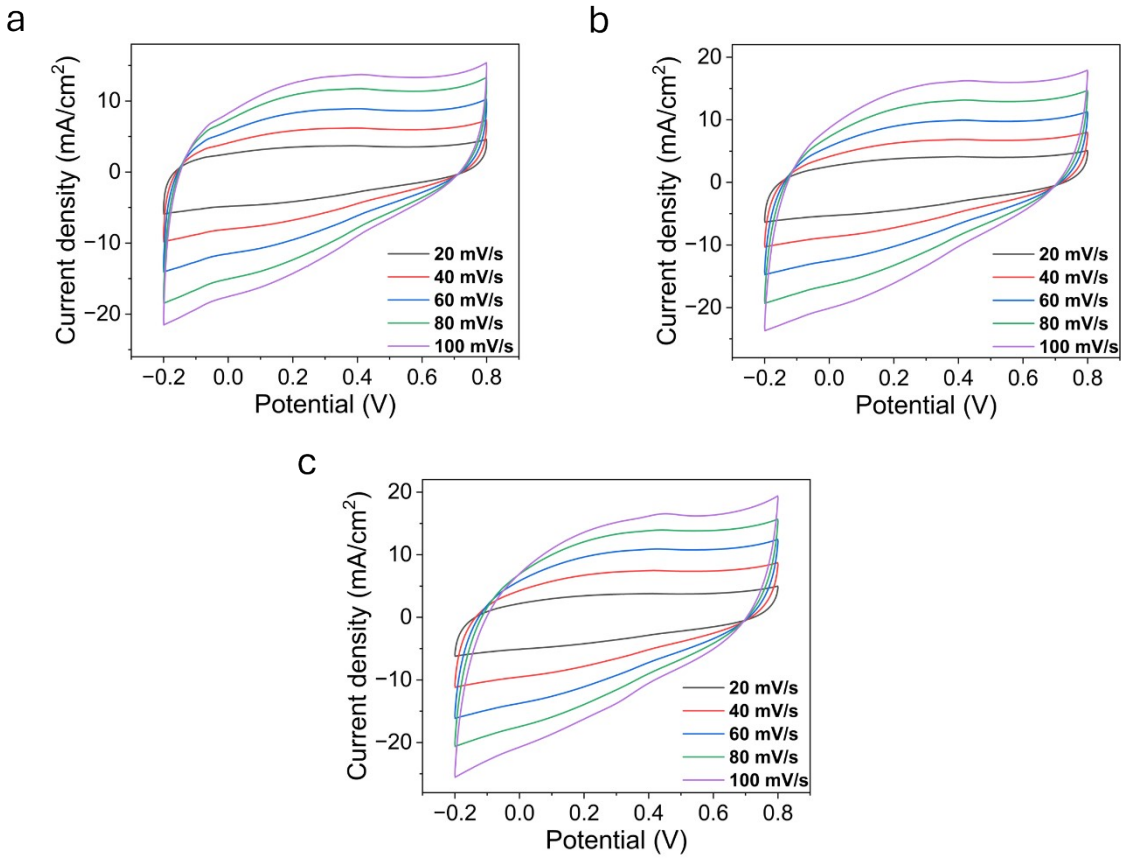

Figure. S3 Cyclic voltammetry (CV) curves of **(a)** LIG-P0, **(b)** LIG-P60, and **(c)** LIG-P100 electrodes collected at various scan rates ranging from 20 to 100 mV/s.

To assess the universality of the electrochemical behavior across different electrode configurations, the CV profiles of LIG-P0, LIG-P60, and LIG-P100 were systematically compared (***Figure S3***). Consistent with the optimal LIG-P80 electrode discussed in the main text, all three samples exhibit characteristic quasi-rectangular shapes without noticeable redox peaks. This confirms that the charge storage mechanism is dominated by electric double-layer capacitance (EDLC) and remains fundamentally unchanged by the laser drilling process. Furthermore, even at a high scan rate of 100 mV/s, the curves retain their rectangular symmetry with minimal distortion. This indicates that the monolithic graphene framework maintains excellent electrical conductivity and structural stability, ensuring efficient charge transfer regardless of the specific channel diameter.

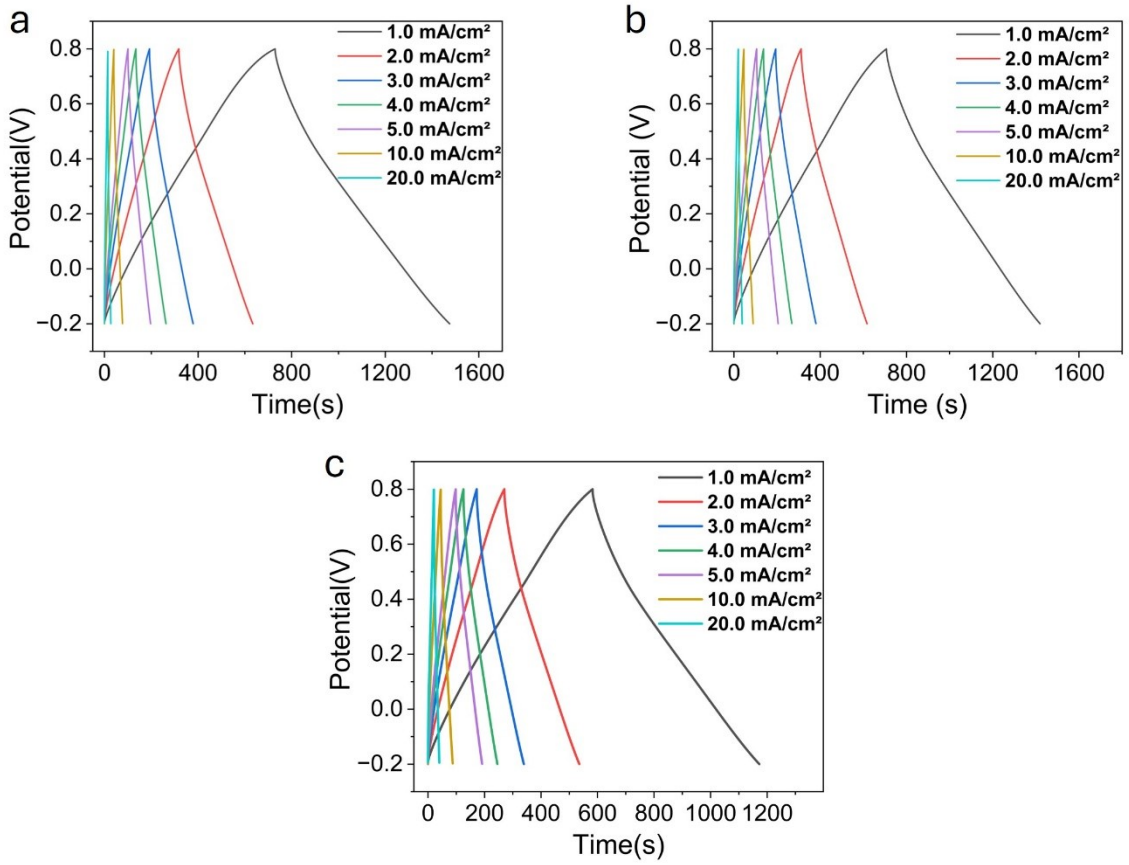

Figure. S4 Galvanostatic charge-discharge (GCD) curves of (a) LIG-P0, (b) LIG-P60, and (c) LIG-P100 electrodes measured at various current densities ranging from 1.0 to 20.0 mA/cm².

To further verify the rate capability and charge storage reversibility, the galvanostatic charge-discharge (GCD) profiles of LIG-P0, LIG-P60, and LIG-P100 were evaluated (Figure S4). All electrodes display highly linear and symmetric triangular shapes across the entire current density range (1.0 to 20.0 mA/cm²), characteristic of ideal electric double-layer capacitance (EDLC) behavior. The linear voltage-time relationship indicates a constant capacitance during the charging and discharging processes. Notably, even at a high current density of 20.0 mA/cm², the curves show negligible IR drop (voltage drop at the initiation of discharge), which further corroborates the low internal resistance and excellent electrical continuity of the monolithic porous framework.

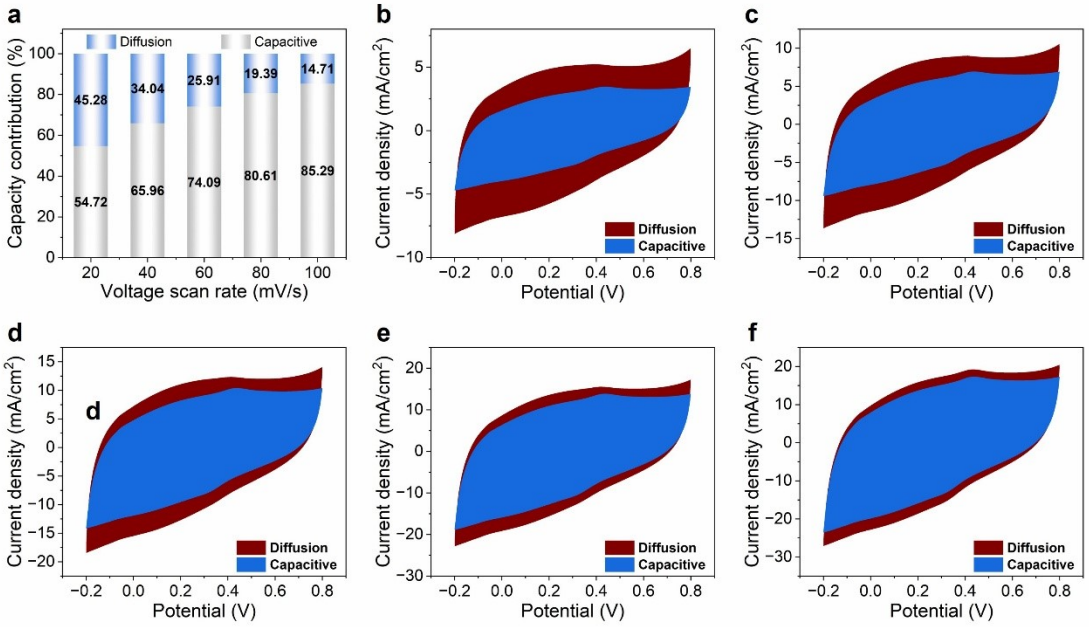

Figure. S5. Dunn analysis of the representative LIG-P80 electrode. (a) Capacitive and diffusion-controlled contribution ratios at different scan rates. (b–f) Separation of the total current response into capacitive contribution (blue) and diffusion-controlled contribution (red) at 20, 40, 60, 80, and 100 mV/s, respectively.

To further clarify the charge-storage behavior of the representative LIG-P80 electrode, Dunn's analysis was performed based on CV curves collected at different scan rates. According to the relationship i(V)=k1v+k2v1/2, the current response can be separated into a capacitive contribution and a diffusion-controlled contribution. As shown in Fig. S5a, the capacitive contribution gradually increases from 54.72% at 20 mV/s to 65.96%, 74.09%, 80.61%, and 85.29% at 40, 60, 80, and 100 mV/s, respectively, while the diffusion-controlled contribution correspondingly decreases from 45.28% to 34.04%, 25.91%, 19.39%, and 14.71%. The separated current responses shown in Fig. S5b–f further confirm that charge storage in LIG-P80 is governed by a mixed mechanism, with an increasingly dominant surface-controlled capacitive contribution at higher scan rates. Notably, such a high capacitive contribution for a macroscopic thick electrode indicates that the architected micro-channel topology effectively shortens the characteristic ion-transport distance from the electrode thickness scale to a much smaller radial diffusion

scale, thereby preserving the kinetic accessibility of deep active surfaces and supporting the excellent rate capability of the channel-architected thick electrode

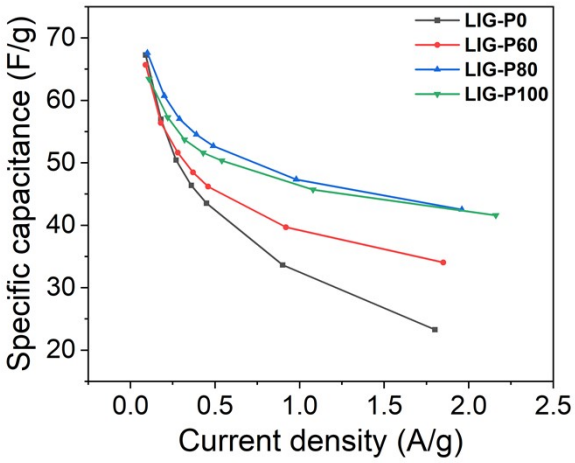

Figure. S6. Converted gravimetric capacitance of different thick electrodes as a function of the equivalent gravimetric current density.

To further assess the reactivation of the kinetically inaccessible "dead volume" in thick electrodes, the gravimetric capacitances and the corresponding equivalent gravimetric current densities were converted from the areal electrochemical data using the experimentally measured areal mass loading of each electrode, and the corresponding results are summarized in Fig. S6. As shown in Fig. S6, LIG-P80 delivers 67.58 F/g at 0.10 A/g and retains 42.51 F/g at 1.96 A/g, outperforming LIG-P0 over the entire tested range. These mass-normalized results indicate that the laser-architected microchannels improve the utilization of active material, especially at high rates, thereby supporting the mitigation of the "dead volume" effect in thick electrodes.

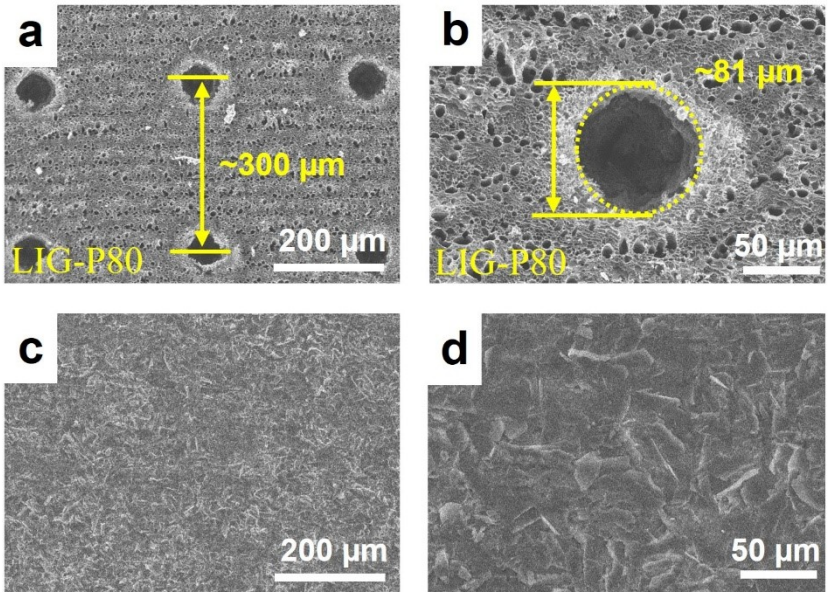

Figure. S7. Post-cycling SEM images of the LIG-P80//Zn device electrodes after 20,000 cycles. (a, b) LIG-P80 cathode. (c, d) Zn anode.

To evaluate the structural robustness of the channel-architected thick electrode during prolonged cycling, post-cycling SEM characterization was performed on both the LIG-P80 cathode and the Zn anode after 20,000 charge-discharge cycles. As shown in Fig. S7a, the arrayed micro-channel pattern of the LIG-P80 cathode remains clearly recognizable over a large area, and the inter-channel spacing is well maintained at ~300 μm. The high-magnification image in Fig. S7b further shows that the channel contour remains distinct, with a characteristic diameter of ~81 μm. No obvious structural collapse, severe pore blockage, or significant mechanical damage is observed after long-term cycling, indicating good structural integrity of the vertically aligned micro-channel architecture. In addition, the cycled Zn anode was also examined, as shown in Fig. S7c,d. The Zn surface exhibits a relatively uniform roughened morphology with flake-like surface features after prolonged cycling. No obvious large-scale needle-like dendrites, severe cracking, or catastrophic surface degradation are observed at the present magnifications, suggesting acceptable interfacial stability of the Zn anode during repeated Zn plating/stripping.

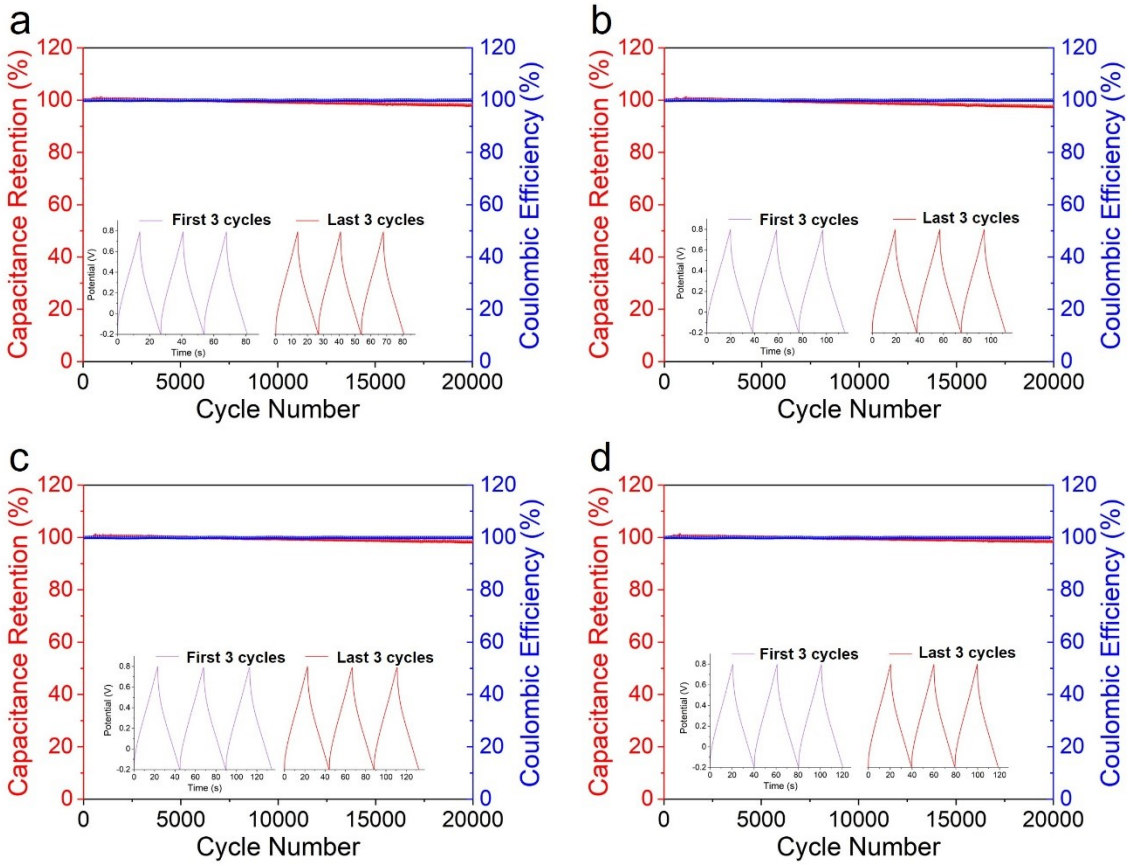

Figure. S8. Long-term cycling performance of different thick electrodes at 20 mA/cm²: (a) LIG-P0, (b) LIG-P60, (c) LIG-P80, and (d) LIG-P100. The red curves represent capacitance retention and the blue curves represent coulombic efficiency. Insets show the first 3 cycles and the last 3 cycles.

To complement the long-term cycling results presented in Fig. 4g of the main text, the corresponding capacitance-retention and coulombic-efficiency curves of the different thick electrodes are summarized in Fig. S8. As shown in Fig. S8a–d, all electrodes maintain coulombic efficiencies close to 100% throughout the 20,000-cycle test at 20 mA/cm², indicating highly reversible charge-storage behavior and good electrochemical stability. Meanwhile, the capacitance-retention trends are consistent with the specific-capacitance evolution shown in Fig. 4g, further confirming the good cycling durability of the laser-architected electrodes. The insets display the first 3 cycles and the last 3 cycles, showing that the charge/discharge profiles remain largely symmetric after prolonged cycling.

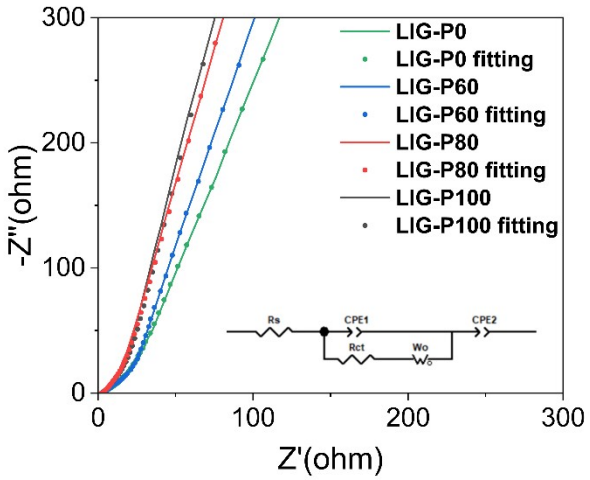

Figure. S9 Experimental and fitted Nyquist plots of LIG-P0, LIG-P60, LIG-P80, and LIG-P100 electrodes.

Table S1 Electrochemical impedance parameters (Rs, Rct, and Wo) obtained by fitting the EIS data to the equivalent circuit model

Sample	Rs（Ω）	Rct（Ω）	Wo（Ω）
LIG-P0	2.18	0.21	106.84
LIG-P60	2.26	0.28	92.57
LIG-P80	2.14	0.29	68.15
LIG-P100	2.19	0.29	60.85

To quantitatively decouple the resistive components within the thick electrode architecture, the EIS spectra were fitted using an equivalent circuit model (Modified Randles Circuit) composed of the equivalent series resistance (Rs), charge transfer resistance (Rct), Warburg diffusion impedance (Wo), and constant phase elements (CPE), as shown in the inset of Figure S9. The fitting results, summarized in Table S1, reveal two critical trends.

First, the Rs values for all laser-drilled samples (2.14–2.26 Ω) remain highly comparable to that of the pristine LIG-P0 (2.18 Ω). This confirms that the subtractive laser manufacturing preserves the integrity of the conductive graphene network without causing electrical isolation.

Second, and most importantly, the Warburg impedance (Wo), which represents the ion diffusion resistance within the porous electrode, shows a sharp dependence on channel geometry. The Wo value decreases significantly from 106.84 Ω (LIG-P0) to 68.15 Ω (LIG-P80) and 60.85 Ω (LIG-P100). This 43% reduction in diffusion resistance for LIG-P100 provides direct quantitative evidence that the vertical micro-channels successfully minimize the tortuosity of the transport path, thereby effectively mitigating the diffusion limitations inherent in thick electrodes.

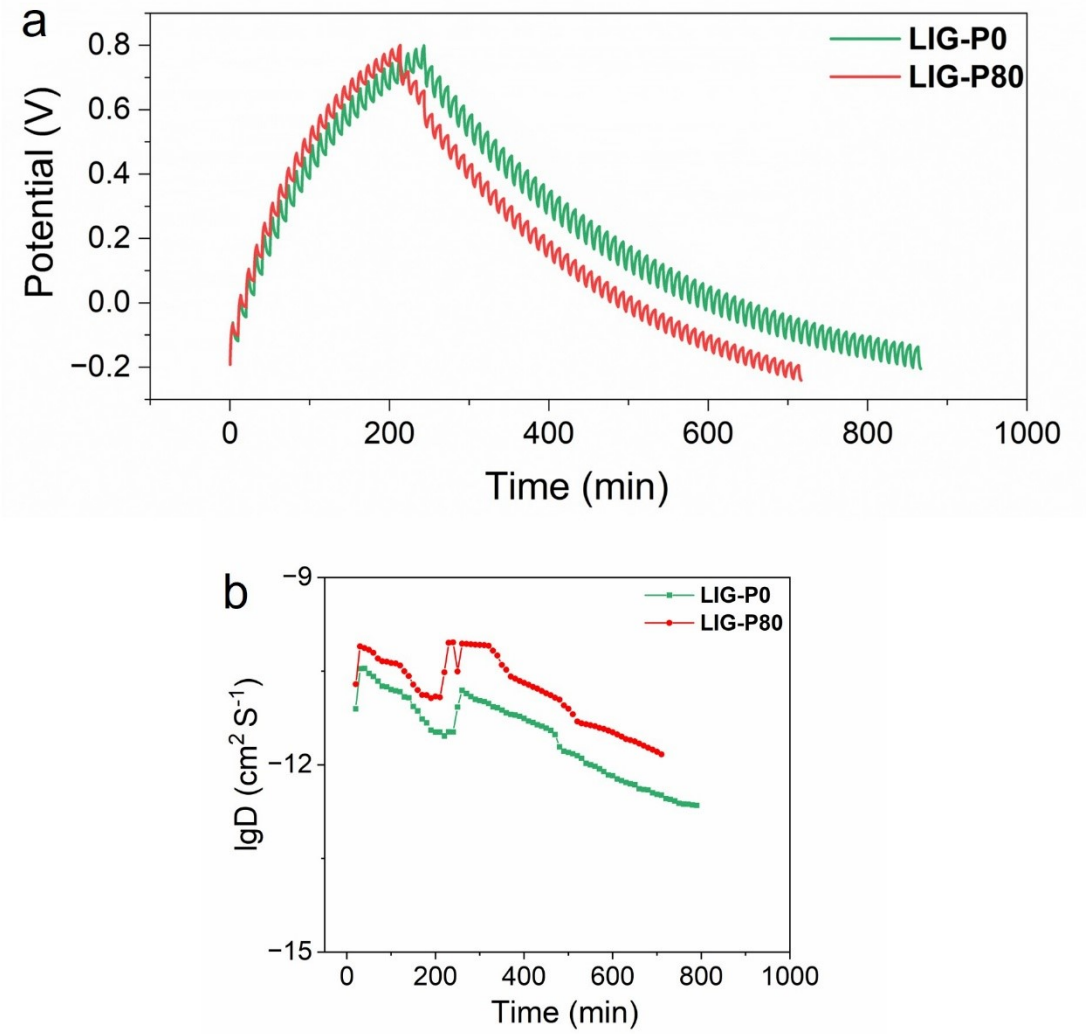

Figure. S10. GITT analysis of the representative thick electrodes. (a) GITT potential profiles of the LIG-P0 and LIG-P80 electrodes measured in the potential window of −0.2 to 0.8 V under a pulse/relaxation protocol of 50 s galvanostatic polarization followed by 100 s open-circuit relaxation. (b) Apparent ion diffusion coefficients (lgD) derived from the corresponding GITT responses as a function of time.

To further evaluate the ion-transport kinetics associated with the deep-pore transport limitation, GITT measurements were performed on the representative LIG-P0 and LIG-P80 electrodes, and the corresponding results are summarized in Fig. S10. The measurements were carried out at a current density of 0.1 mA/cm² in the potential window of −0.2 to 0.8 V using a pulse/relaxation protocol of 50 s galvanostatic polarization followed by 100 s open-circuit relaxation. As shown in Fig. S10a, the two electrodes

exhibit distinct potential-evolution behaviors under the same testing conditions. Compared with LIG-P0, the LIG-P80 electrode shows a faster overall potential response during the charge/discharge process. Based on the GITT profiles, the apparent ion diffusion coefficients were further estimated, and the corresponding lgD values are plotted in Fig. S10b. It can be seen that LIG-P80 maintains consistently higher lgD values than LIG-P0 over most of the tested range, indicating faster ion-transport kinetics in the channel-architected thick electrode. These results further support that the arrayed vertical channels effectively alleviate the deep-pore transport limitation by shortening the ion-transport pathway and improving the accessibility of the deep active regions.

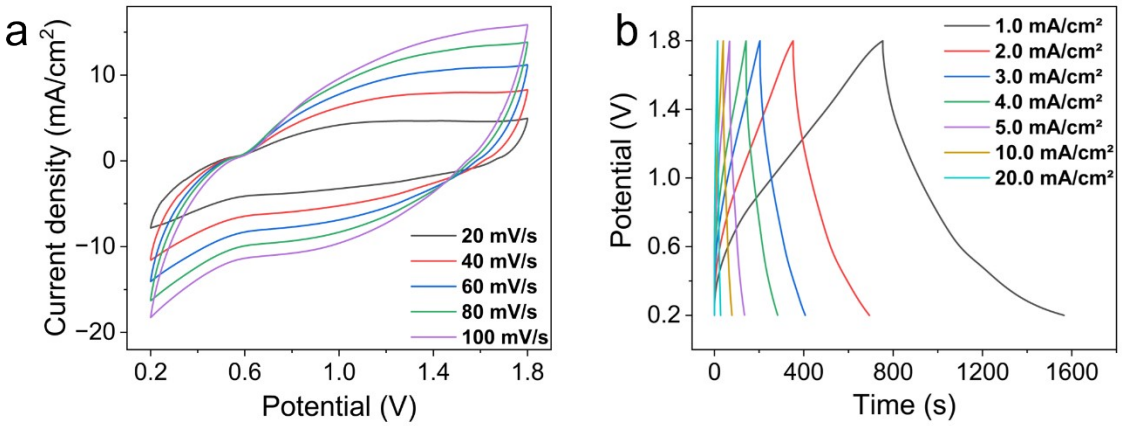

Figure. S11 Electrochemical performance of the zinc-ion hybrid capacitor based on the pristine LIG-P0 cathode (LIG-P0//Zn). (a) CV curves recorded at scan rates ranging from 20 to 100 mV/s. (b) GCD curves measured at current densities from 1.0 to 20.0 mA/cm².

To establish a performance baseline for evaluating the impact of the vertical channel arrays, the electrochemical behavior of the control device assembled with the pristine LIG-P0 cathode (LIG-P0//Zn) was characterized (Figure S11). The CV curves (Panel a) display characteristic capacitive envelopes within the voltage window of 0.2–1.8 V. However, compared to the optimized LIG-P80 device (presented in Figure 6b of the main text), the LIG-P0 device exhibits more pronounced shape distortion and polarization at high scan rates (e.g., 100 mV/s). This "leaf-like" distortion indicates higher internal resistance and

sluggish ion transport kinetics inheren the thick, non-channeled electrode architecture. Similarly, while the GCD profiles (Panel b) maintain triangular shapes, they demonstrate limited discharge capacities compared to the channeled electrodes, confirming that the lack of vertical pathways restricts the accessibility of active sites deep within the porous framework

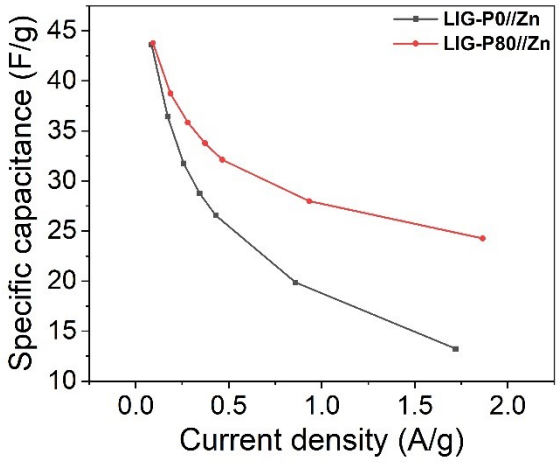

Figure. S12. Gravimetric capacitance of the LIG-P0//Zn and LIG-P80//Zn devices as a function of the equivalent gravimetric current density, recalculated from the areal capacitance data using the total active mass of the cathode together with an equivalent Zn anode mass under an N/P ratio of 2.

For device-level comparison, the gravimetric capacitances of the LIG-P0//Zn and LIG-P80//Zn devices were recalculated from the areal capacitance data using the total active mass of the cathode together with an equivalent Zn anode mass under an N/P ratio of 2[3-5], and the corresponding results are summarized in Fig. S12. Under this mass-normalized criterion, the LIG-P80//Zn device delivers 43.77 F/g at 0.093 A/g and retains 24.26 F/g at 1.866 A/g. Across the tested range, the LIG-P80//Zn device maintains higher gravimetric capacitance than the LIG-P0//Zn device, particularly at high current densities. In addition, based on the same mass-normalized criterion, the LIG-P80//Zn device achieves a gravimetric energy density of 15.56 Wh/kg and a gravimetric power density of 1494.0 W/kg.

Figure. S13 Digital photograph demonstrating the practical viability of the LIG-P80//Zn hybrid capacitor.

To further verify the practical application potential of the laser-architected thick electrodes, a soft-packaged zinc-ion hybrid capacitor was assembled using the optimal LIG-P80 cathode and a Zn foil anode. As shown in Figure S13, the fully charged device effectively powers a red light-emitting diode (LED), confirming its capability to deliver stable voltage and current output. This demonstration serves as a tangible proof-of-concept, validating that the high areal energy density and power density calculated from electrochemical measurements can be effectively translated into real-world utility for driving portable electronic devices

Table. S2 Performance comparison of the LIG-P80//Zn device with representative aqueous zinc-ion hybrid supercapacitors reported in the literature.

Electrode materials	Potential window	C_A	E_A (mWh/cm^2)	P_A (mW/cm^2)	Cycling life (Cycle number)	Refer
LIG	0.2-1.8 V	415.2 mF/cm^2(2 mA/cm^2)	0.1668	16	95.1% (20000)	**This work**
$Zn(CF_3SO_3)_2$-PAM	0.1-1.7 V	196.7 mAh/g(0.1A/g)	0.0082	0.04	95%(100)	[6]
Ti3C2Tx	0-1.4 V	72.02 mF/cm^2(10 mV/s)	0.02	0.5	80 (50000)	[7]
CNT	0.2-1.8	83.2 mF/cm2(1 mA/cm^2)	0.0296	0.8	87.4 (6000)	[8]
V_2CT_x	0-1.6 V	200.1 mF/cm2(0.5 mA/cm^2)	0.0716	0.4	88.9% (5000)	[9]
MoS_2/rG	0.2-1.3 V	93.5 mF/cm^2(10 mV/s)	0.00165	1.97	94.6%(800)	[10]
Ppy/GO-AM	0-1.6 V	125 mF/cm^2 (1mA/cm^2)	0.0444	0.8	90.3(5000)	[11]
$NbP_2O_7/Ti_3C_2T_x$	0-1.6 V	56.65 mF/cm^2 (3mA/cm^2)	0.0125	0.085	95%(8500)	[12]

To further evaluate the practical competitiveness of the LIG-P80//Zn device, a comparison with representative aqueous zinc-ion hybrid supercapacitors reported in the literature is summarized in Table S2. Key device-level metrics, including potential window, areal specific capacitance, areal energy density, areal power density, and cycling stability, are listed for direct comparison. The results show that the LIG-P80//Zn device

delivers a competitive combination of high areal energy/power output and excellent long-term cycling durability.

Reference

[1] Y. Liu, S. Zheng, J. Ma, X. Wang, L. Zhang, P. Das, K. Wang and Z.-S. Wu, *Adv. Energy Mater.*, 2022, **12**, 2200341.

[2] Y. Zheng, W. Zhang, X. Zhu, F. Liu, C. Yang and W. Zheng, *J. Am. Chem. Soc*., 2024, 146, 20291–20299.

[3] J. Wu, D. Zhu, Y. Pan, J. Prabowo, L. Wei and Y. Chen, Adv. Sci., 2024, 11, 2408997.

[4] J. Zhu, J. Tai, T. Liu, Y. Wang, Y. Li, M. Yang, D. Ma, L. Deng, J. Luo and P. Zhang, Adv. Energy Mater., 2025, 15, 2403739.

[5] L. Yao, N. Koripally, C. Shin, A. Mu, Z. Chen, K. Wang and T. N. Ng, Nat. Commun., 2025, 16, 3597.

[6] T. Feng, X. Cao, T. Li, R. Diao, Y. Jing, X. Zhang and J. Zhu, Energy Technol., 2026, 14, e202501129.

[7] J. Zeng, L. Dong, L. Sun, W. Wang, Y. Zhou, L. Wei and X. Guo, Nano-Micro Lett., 2021, 13, 19.

[8] L. Li, W. Liu, K. Jiang, D. Chen, F. Qu and G. Shen, Nano-Micro Lett., 2021, 13, 100.

[9] G. Sun, H. Yang, G. Zhang, J. Gao, X. Jin, Y. Zhao, L. Jiang and L. Qu, Energy Environ. Sci., 2018, 11, 3367–3374.

[10] T. Huang, B. Gao, S. Zhao, H. Zhang, X. Li, X. Luo, M. Cao, C. Zhang, S. Luo, Y. Yue, Y. Ma and Y. Gao, Nano Energy, 2023, 111, 108383.

[11] H. Sheng, L. Jiang, Q. Wang, Z. Zhang, Y. Lv, H. Ma, H. Bi, J. Yuan, M. Shao, F. Li, W. Li, E. Xie, Y. Liu, Z. Xie, J. Wang, C. Yu and W. Lan, Sci. Adv., 2023, 9, eadh8083.

[12] Y. Wu, W. Yuan, P. Wang, X. Wu, J. Chen, Y. Shi, Q. Ma, D. Luo, Z. Chen and A. Yu, Adv. Sci., 2024, 11, 2308021.

[13] A. M. Patil, H.-M. You, A. A. Jadhav, J. Hong, S. K. Das, S. D. Dhas, T. J. Lim, E. Lee, K. Y. Chung, K. Kim and S. C. Jun, Adv. Energy Mater., 2025, 15, 2403322.